Guoyu Li ✉
Yexuan Luo

https://doi.org/10.21278/TOF.494073324
ISSN 1333-1124
eISSN 1849-1391

COMPRESSION CHARACTERISTICS OF SORGHUM STRAW BASED ON ITS MICROSTRUCTURE AND INVERSE RECONSTRUCTION

Summary

The structural properties of sorghum straw, a sustainable biomass, make it a promising material for applications in agricultural machinery and thin-walled tube bionics. This study analysed its microstructure using scanning electron microscopy (SEM) and inverse reconstruction, creating both composite and simplified 3D models. Finite element simulations revealed axial and radial compression characteristics, with the outer skin bearing higher stresses (up to 4,304 MPa) than the foam-like pith core. Vascular bundles, dispersed within basic tissues, vary in size and number across layers, contributing to the structural integrity of the straw. Experimental validation showed that the 3D composite model closely matched stress distribution to compression behaviour, with errors below 15%. The findings offer insights into mechanical properties of sorghum straw, supporting its application in biomedicine, bionics, and engineering.

Key words: *sorghum straw; microstructure; inverse reconstruction; compression characteristics; finite element simulation*

1. Introduction

Crop straw has emerged as a pivotal renewable material in sustainable engineering applications, and the relationship between its microstructure and mechanical properties has come into focus. In recent studies, Liu et al. determined the growth-stage-dependent cutting characteristics of oil peony stalks through a microstructural evolution analysis [1], Kong et al. identified vascular bundle configuration as a key determinant of wheat stalk buckling resistance [2], and Shah et al. demonstrated that mechanical tissue thickness inversely correlates with vascular bundle density in high-strength wheat stalks [3]. SEM-based comparative studies further confirmed interspecies microstructural variations impacting mechanical performance [4].

Mechanical characterisation methodologies have significantly advanced through the finite element modelling of maize stover transverse modulus developed by Stubbs et al. [4], the evaluation of Faborode/Maxwell models in compression-relaxation profiling [5, 6], and a comparative study on elastic modulus measurement techniques [7]. Parallel progress in bio-inspired design includes the cutting parameter optimisation by Mathanker et al. [8], the wind-resistant multicellular structure discovery in cattail leaves [9], and the cattail-inspired energy absorption systems [10]. Particularly noteworthy are biomimetic breakthroughs achieving 17% specific energy absorption (SEA) improvement through staggered pearl-layer simulations [11],

cattail-node carbon fibre reinforced plastic (CFRP) tubes [12], diatom-inspired cushion pads [13], and coconut palm-mimetic tubular bellows [14-16].

Despite these advances, the structural potential of sorghum straw remains underexplored, particularly regarding its nodal microstructure - a critical feature differentiating it from conventional straw materials [17-18]. Our study addresses this gap through: (1) SEM-validated 3D reconstruction of nodal microarchitecture, (2) development of multi-fidelity finite element analysis (FEA) models (composite vs. simplified), (3) systematic comparison of axial/radial compression mechanisms. This tripartite approach enables unprecedented correlation between hierarchical microstructures and macroscopic energy absorption performance, establishing a biomimetic design framework validated through experimental compression tests.

2. Microstructural analysis of sorghum stalks

2.1 Samples

Eight straw samples of the sorghum variety Ugnu were collected in Jiaozuo City, Henan Province, China, from healthy, pest- and disease-free straws grown during the current year (Fig. 1). The straw showed no visible defects, epidermal damage, or cracks. To study the characteristics of the straw nodes, the samples were taken 9 mm above and 9 mm below the nodes, with a diameter of approximately 20 mm. The fresh stems initially had a moisture content of 68-72% (wet basis). Prior to testing, the samples were air-dried in a controlled environment (25°C, 40% RH) for 72 hours, followed by oven-drying at 50°C until reaching the equilibrium weight. This standardised drying protocol was adopted to eliminate moisture-induced variability during the mechanical characterisation, as commonly practiced in lignocellulosic material studies.

Fig. 1 Sorghum straw test samples

2.2 Scanning electron microscope

In this study, the microstructural analysis was performed using a Zeiss EVO-18 scanning electron microscope from Germany. Its key parameters include an adjustable accelerating voltage ranging from 1 kV to 30 kV, an experimental magnification range of 13 to 50,000 times, and a minimum resolution of 3.0 nm. Before conducting the SEM experiments, the samples underwent a thorough preparation process, which included gold coating, mounting onto the microscope stage, image acquisition, and data processing. The straw samples were first frozen using liquid nitrogen, then cut, and clear microscopic images were obtained by adjusting the voltage and current for an optimal performance analysis and application.

2.3 Microdistribution

Sorghum straw is composed of an outer bark, basic tissues, and vascular bundles. The vascular bundles are dispersed throughout the basic tissues, as shown in Fig. 2. Moving from the inner to the outer regions of the straw, the size of the vascular bundles decreases while their number increases. Small vascular bundles are primarily distributed in the inner region of the straw (Fig. 2a-b), whereas larger vascular bundles are more prevalent in the outer region

(Fig. 2c-d). The pith core exhibits a foamy cavity structure, with a uniform texture throughout. This foamy matrix completely fills the space within the outer bark. At the nodes, the outer bark thickens in a stepped pattern, and the foamy basic tissue tightly adheres to it (Fig. 2e-f). The diameter of the vascular pores is approximately 20 μm.

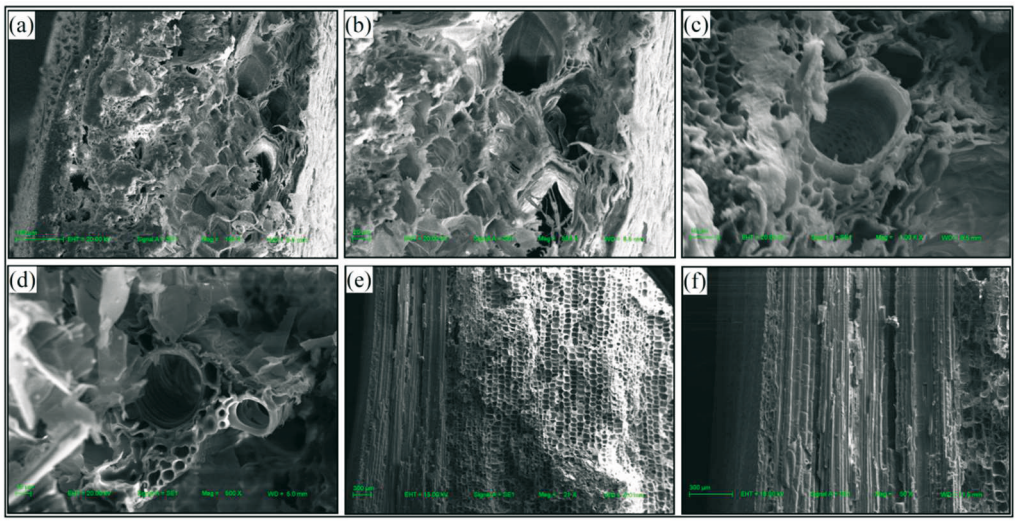

Fig. 2 Microstructure of sorghum straw: (a-b) hollow structure of small vascular bundles; (c-d) hollow structure of large vascular bundles; (e-f) tightly bound outer epidermis and pith core

The vascular bundles of sorghum straw are not entirely straight at the nodes. These bundles are composed of conduits and fibre cells, and at the nodes, the fibre cells are more loosely arranged while the conduits are denser, causing the vascular bundles to curve. This curvature is especially pronounced in the smaller outer vascular bundles (Fig. 3a-c). In contrast, at the internodes, the fibre cells are more tightly packed and the conduits are sparser, allowing the vascular bundles to remain straighter (Fig. 3d-f).

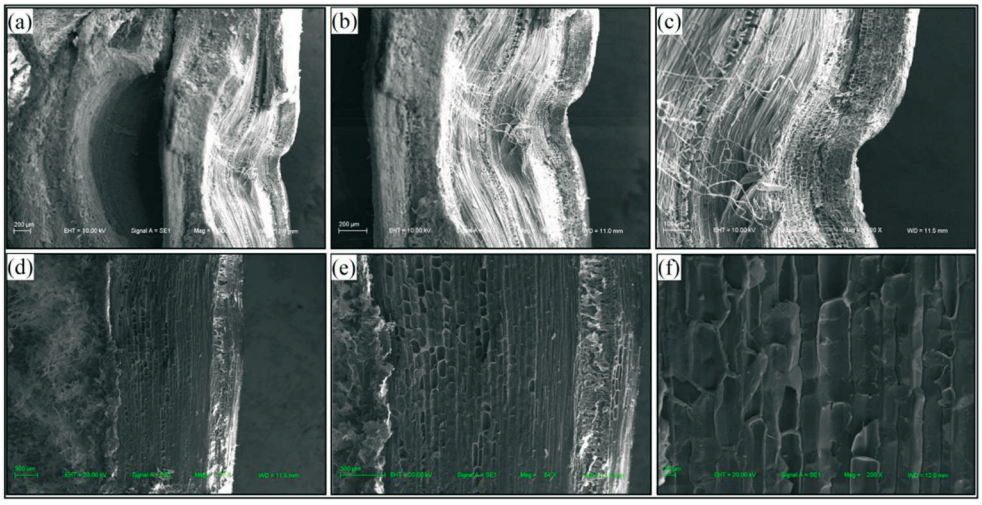

Fig. 3 Microstructure of vascular bundles: (a-c) hollow structure of small vascular bundles; (d-f) hollow structure of large vascular bundles

3. Reverse reconstruction of sorghum straw structure

3.1 Data acquisition

Nodal transition zones of disease-free sorghum straws (moisture content <6%) were scanned using a medical μCT50 system (Scanco Medical AG) with 0.5 μm nominal resolution.

The scanner operated at 90 kVp maximum voltage with a 3,400×1,200 charge-coupled device (CCD) detector, generating 1,795 non-overlapping slices in the digital imaging and communications in medicine (DICOM) format (50×120 mm scan area) at <0.25 μSv/h surface radiation dose. Specimens were strategically selected to encompass intra-/inter-nodal structural gradients along the longitudinal axis, ensuring a comprehensive capture of vascular bundle transitions and parenchyma matrix variations. The raw datasets archived on CD-ROMs provided the foundation for developing multiscale 3D composite models integrating macroscopic computed tomography (CT) reconstructions with SEM-resolved microstructural features [17].

3.2 Reverse straw reconstruction

The reconstruction workflow in Mimics 19.0 initiated with a triplanar alignment of CT datasets (axial/coronal/sagittal views), enabling real-time 3D coordinate synchronisation during image inspection. Preprocessing involved dynamic window-level adjustment (width: 1,500-3,000 HU; level: 500-800 HU) to enhance the tissue contrast, followed by anisotropic diffusion filtering to suppress high-frequency noise while preserving vascular bundle boundaries.

The threshold segmentation (-1,000 to -784 HU) coupled with region-growing algorithms enabled a hierarchical extraction of three structural components: the dense epidermal/fibre layer (gray value: -784±35 HU), vascular network (-920±40 HU), and porous pith core (-1000±50 HU). This density-based stratification was validated against the SEM-observed microanatomy, confirming the threshold accuracy in separating lignified fibres from parenchymatous tissues [18]. The post-segmentation mask editing removed carrier platform artifacts before 3D model calculation, generating watertight STL surfaces preserving topological continuity across nodal regions.

The composite model (Fig. 4) synthetically combined the CT-derived macroscale geometry (vascular bundle spatial distribution, epidermal curvature) with the SEM-informed microscale attributes (fibre orientation angles, pit membrane porosity). The spatial registration between CT and SEM datasets achieved <2 μm alignment error through the landmark-based affine transformation, ensuring multiscale structural fidelity. The final models retained critical biomechanical features, including anisotropic vascular bundle reinforcement and graded foam core density profiles essential for subsequent FEA simulations.

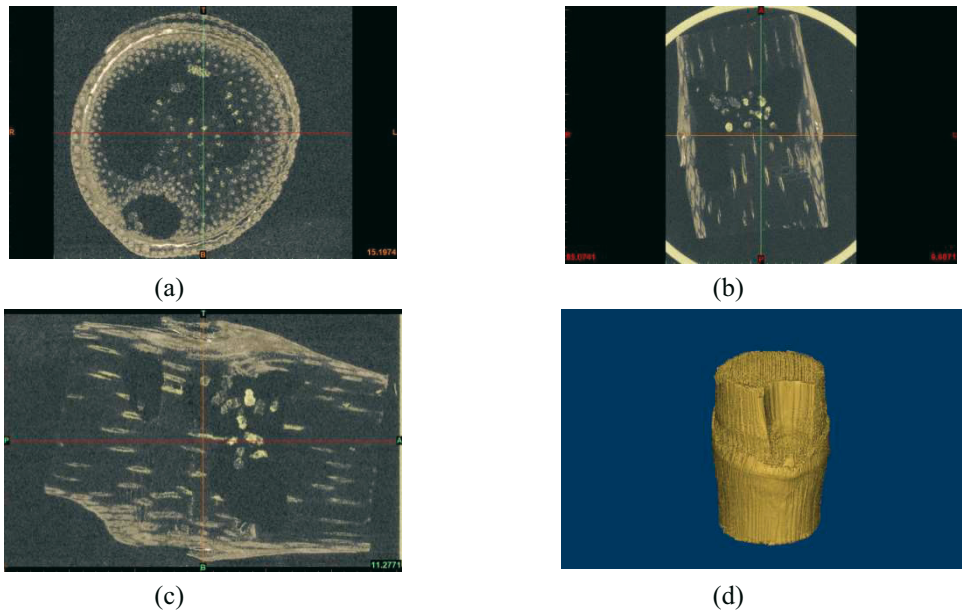

(a) (b) (c) (d)

Fig. 4 3D reconstructed model of sorghum straw: (a) front view; (b) top view; (c) side view; (d) 3D reconstructed model

To create a composite model that encompasses the outer skin of the straw, vascular bundles, and the inner foam pith core, a three-dimensional composite model for each straw component was developed in this study. This model is based on the overall structure of a single material obtained through inverse reconstruction, complemented by the microstructure of the straw observed via SEM.

4. Simulation model construction and conditions

While SEM effectively resolves cross-sectional morphological features, it fails to delineate three-dimensional vascular bundle orientation and nodal fibre distribution with sufficient fidelity. This limitation is addressed through micro-CT-based inverse reconstruction, which precisely maps internal fibre trajectories (0.5 μm resolution) to establish biomimetically accurate nodal structural features [19]. However, the inherent system noise (>45 dB SNR) compromises the surface integrity, rendering the raw reconstructed model unsuitable for finite element meshing. To reconcile the multimodal advantages, a hybrid modelling paradigm was developed: SolidWorks-based 3D composite integration of the SEM-resolved epidermal topology (including step-like nodal thickening patterns) with the μCT-derived vascular hierarchy enables faithful representation of both macro-scale epidermal dimensions (axial thickening ratio: 38.7%) and micro-scale bundle distribution gradients. As illustrated in Fig. 5, the optimised model retains critical architectural elements, i.e. a radially graded vascular system (inner bundles: Ø850±120 μm; outer bundles: Ø220±50 μm), a homogeneous foam matrix (88±7% pore occupancy), and nonlinear bundle organisation exhibiting spatial heterogeneity (internode alignment: 12.7° angular deviation vs. nodal bifurcation: 38.4°). This synthesis of multiscale structural intelligence ensures computational readiness for subsequent biomechanical simulations while preserving the organism's intrinsic load-adaptive morphology.

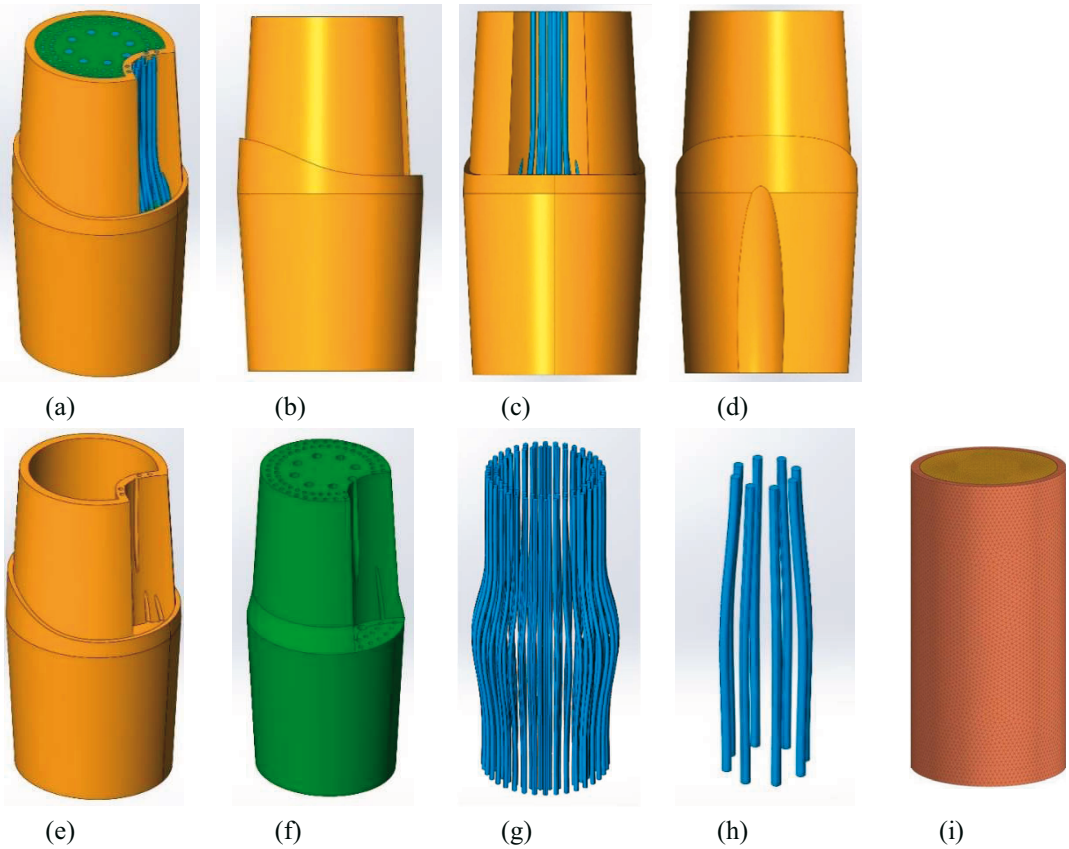

Fig. 5 View of the sorghum straw composite model: (a) axonometric view; (b-c) side view; (d) front side view; (e) outer skin; (f) foam matrix; (g) outer small fibres; (h) inner large fibres; (i) simplified model of sorghum straw

To facilitate the comparison with the 3D composite model and support subsequent engineering applications, a simplified CAD model of sorghum straw was developed [20], as shown in Fig. 5(i). In this simplified model, the straw is assumed to be a double-layer orthotropic anisotropic material. The material structure is considered symmetric, and local variations in radial dimensions at the nodes are disregarded, treating the material as structurally straight. In this model, the fibres are arranged uniformly along the axial direction. Based on the structural characteristics of the straw, it is represented as a laminated composite structure composed of two components: the outer skin and the core. The basic shape of the model combines a regular cylinder with a hollow cylinder.

4.1 Axial compression simulation

4.1.1 Material properties

Organismal tissues consist of a diverse array of cells, intercellular matrices, and other microstructures that exhibit non-uniform, non-linear, and anisotropic mechanical properties. Currently, it is common practice to approximate the segmentation of biological tissues as structurally homogeneous, isotropic, or anisotropic materials. In biomechanics, the finite element method relies on several foundational assumptions, namely isotropy, homogeneity, and continuous linear elasticity.

Due to the absence of compression instruments for straw, the decision was made to determine E_2, μ_2, and G_2 by calculating the elastic constants through comparisons with those of sugarcane, wheat, wood, and oilseed rape stalks.

The straw bark and pith analysed in this study involve a total of nine elastic parameters, which cannot be directly determined due to limitations in testing equipment and methodologies. Therefore, this paper employs a combination of the composite material theory and a comparative analysis for parameter selection. According to the composite material theory, the following relationship exists between the elastic modulus and Poisson's ratio of orthotropic anisotropic materials (Equation 1):

$$\begin{cases} \dfrac{\mu_{21}}{E_1} = \dfrac{\mu_{12}}{E_2} \\ \dfrac{\mu_{31}}{E_1} = \dfrac{\mu_{13}}{E_3} \quad \dfrac{\mu_{ij}}{E_j} = \dfrac{\mu_{ij}}{E_i} \ (i, j = 1,2,3.\ i \neq j) \\ \dfrac{\mu_{32}}{E_2} = \dfrac{\mu_{23}}{E_3} \end{cases} \tag{1}$$

where μ is Poisson's ratio and E is the modulus of elasticity.

Based on the studies of actual biomaterials, in anisotropic materials, the shear modulus G is numerically related to the elastic modulus E by a specific order of magnitude (Equation 2):

$$G_{ij} = \left(\frac{1}{3} \sim \frac{1}{2}\right) E_{ij} \ (i, j = 1,2,3.\ i \neq j) \tag{2}$$

In agricultural biomechanics, it is observed that Poisson's ratio for the majority of materials typically ranges between 0.2 and 0.5. Furthermore, Poisson's ratio is also influenced by the magnitude of stress [21]. The actual distribution interval for Poisson's ratio is relatively narrow; for isotropic materials, it is generally around 0.3. Referring to relevant literature that has established the ontological model, in this study, the material parameters for the outer skin and pith core of sorghum straw are selected, as presented in Table 1.

Table1 Definition of elastic parameters for finite element analysis of sorghum straw

Elastic parameter	E_1 /MPa	E_2 /MPa	E_3 /MPa	G_{12} /MPa	G_{23} /MPa	G_{13} /MPa	μ_{12}	μ_{23}	μ_{13}
Epidermis	3845.7	3845.7	7895.62	1479.12	3947.81	3947.81	0.3	0.146	0.146
Pith	41.83	41.83	220.87	16.09	110.44	110.44	0.01	0.0019	0.0019

4.1.2 Mesh division and loading conditions

The CAD model of sorghum straw was saved as an IGS file and imported into the HyperMesh software for meshing. After exporting the mesh model, the material and cross-sectional properties were defined, along with the boundary and load conditions. Finally, the model was imported into LS-DYNA for problem solving [22]. The simulation results were then used to analyse the stress distribution of the straw structure under axial and radial compression.

Given that the straw studied in this paper exhibits a degree of axisymmetry and that the fibres are arranged axially, hexahedral meshing was performed using three-dimensional solid elements (SOLID186) [23]. The free mesh division method was employed, with the cell size set to 0.05 mm. The geometry of the straw resulted in a regular mesh division, and the details regarding the number of mesh cells, mesh cell distribution, and mesh quality are summarised in Table 2.

Table 2 Straw model grid and number of cells

Sorghum straw	Number of nodes		Number of units	
	Simplified model	Composite model	Simplified model	Composite model
Rind	23,073	23,372	85,521	93,207
Foam	23,153	3,101	110,161	62,348
Large vascular bundle (botany)	-	3879	-	9,841
Vascular cambium (botany)	-	21,168	-	31,392

The material and cross-sectional properties as well as the boundary and loading conditions were established to simplify the basic organisation of the sorghum stalk model into a laminated structure composed of vascular bundles and fibre composites [24]. Continuous deformation of the xylem and fibres in the model was achieved through bonding operations. The amount of compression used for axial and radial compression analyses was determined based on experimental data. In testing, the failure of the stalk's intercepted section occurred when the axial and radial compression reached 25% applying a mechanical universal testing machine, indicating that the strain exceeded elastic deformation at 30%. Therefore, in the simulation analysis, the straw was compressed transversely and longitudinally up to 20%.

5. Analysis of simulation results

5.1 Axial compression

Fig. 6 illustrates the axial compression deformation and stress distribution of both the sorghum straw and its simplified model. In Fig. 6(a), the gray area indicates regions of structural failure. Since the pith core has a foam structure, it is less susceptible to damage, as shown in Fig. 6(b). The stress distribution in the outer skin of the sorghum straw resembles that in the pith core, with maximum values occurring at the nodes. Specifically, the maximum stress in the skin is 3,282 MPa, while that in the pith core is 1,565 MPa. During axial compression, the stress in the skin is significantly higher than in the pith core, suggesting that the skin serves as the primary load-bearing component. Under natural conditions, the skin protects the pith core from damage.

Due to the non-circular cross-sectional structure of the sorghum straw, the stress distribution is not uniform in the circumferential direction, with higher stress values observed in the notched regions. In these notched areas of the skin, the stress values range from approximately 458.3 MPa to 733.8 MPa, while in the notched regions of the pith core, they range from about 125 MPa to 300 MPa. Maximum stress values in the straw occur at the nodes, with stress levels appearing lower at the ends and higher in the middle. This can be attributed to the outward bulging tendency of the straw during compression and deformation.

The stresses at the upper and lower ends of the epidermis are 825 MPa to 1,100 MPa and 91.67 MPa to 641.7 MPa, respectively, while those at the upper and lower ends of the pith core are 125 MPa to 200 MPa and 25 MPa to 100 MPa, respectively. The stresses in the upper contact region are greater than those in the lower portion, indicating a higher likelihood of failure in the upper section, which aligns with observations from mechanical tests.

In contrast to the CT model, the simplified CAD model exhibits a more uniform stress distribution due to its regular circular and cylindrical structure, as shown in Fig. 6(c-d). However, by the same failure stress criterion, no distinct failure point is observed in the CAD model.

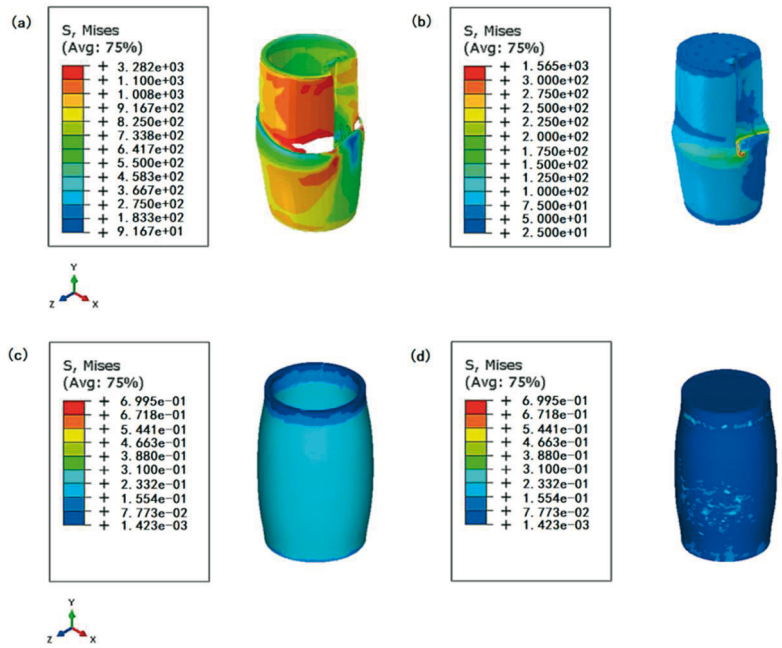

Fig. 6 Axial compression deformation and stress cloud of the sorghum straw and the simplified model: (a) CT reconstruction model of the epidermis; (b) CT reconstruction model of the pith core; (c) simplified CAD model of the epidermis; (d) simplified CAD model of the pith core

5.2 Radial compression

Fig. 7 illustrates the radial compression deformation and stress distribution of both the sorghum straw and its simplified model. In Fig. 7(a), the deformation during the radial compression is primarily concentrated at the expansions on both sides and along the contact line. Multiple gray areas in the figure indicate regions nearing structural failure, particularly at the notches, which aligns with observations from the mechanical testing. The stress distribution in the skin of the sorghum straw resembles that in the pith, with maximum values occurring in the grooves of the nodes and in the contact area with the indenter. The maximum stress in the skin reaches 4,304 MPa, while the maximum stress in the pith is 632 MPa. This significant difference indicates that the outer skin serves as the primary load-bearing component during radial compression.

Given that the pith core is a foam-like porous structure, the stress distribution in the remaining areas is relatively low and uniform, with stress values ranging from approximately 25 MPa to 55 MPa, as shown in Fig. 7(b). The maximum stress occurs at the nodes, and along the stalks, the stresses exhibit a bar-shaped distribution directed along the paracord, converging at the nodes.

In comparison to the composite 3D model, the stress distribution in the simplified 3D model is also more uniform, as depicted in Fig. 7(c) and (d). Similarly, the stresses in this model display a bar-shaped distribution along the growth direction.

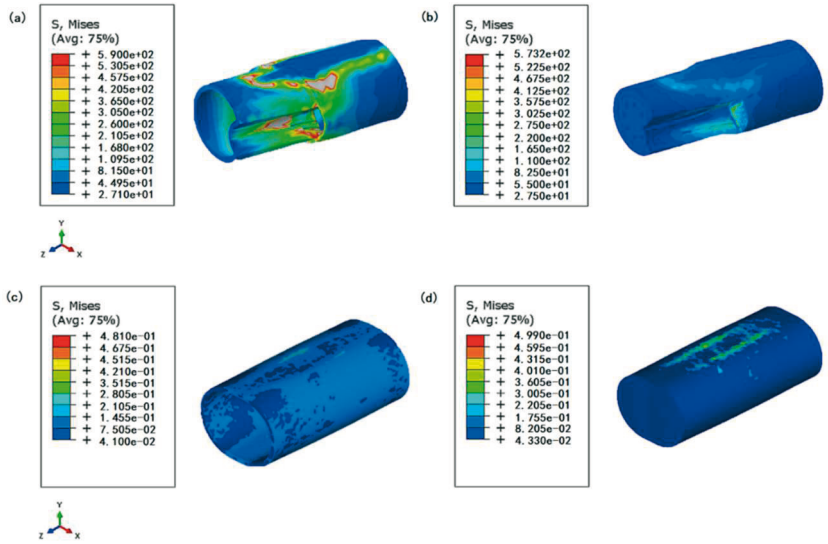

Fig. 7 Radial compression deformation and stress cloud of the simplified model of sorghum straw: (a) CT reconstruction model of the epidermis; (b) CT reconstruction model of the pith core; (c) simplified CAD model of the epidermis; (d) simplified CAD model of the pith core

According to the maximum strain strength criterion for orthotropic anisotropic materials, damage or failure occur when the strain exceeds the material's ultimate strain. Consequently, the simulation results of the CT reconstruction model show skin stress failure, which aligns with the experimental findings. During transverse compression, the elastic modulus of the straw pith is lower than that of the skin, causing the strain to increase sharply from the interior to the exterior along the radial direction. This results in the maximum strain being transmitted to the skin. Additionally, since the skin consists of intertwined axial fibres, the transverse bonding force is considerably weaker than the axial tensile force. As a result, sorghum straw is particularly susceptible to fracture failure under radial compression.

6. Experimental verification of quasi-static mechanics

To verify the accurate determination of the simulated structure, experimental compression tests on sorghum straw are necessary. For this purpose, an ETM-305D (SANS, Shanghai, China) universal testing machine was employed to conduct both axial and radial compression tests, with force displacement curves being collected [25]. This testing machine has a capacity of up to 300 kN, making it suitable for various strength testing requirements, and it boasts an accuracy of 1%. The universal testing machine consists of several components, including the main machine, force transducer, deformation measurement system, control system, data processing system, and operation panel, as illustrated in Fig. 8. Based on a typical force displacement curve and the material mechanics equation (Equation 3), the axial and radial compression strengths were calculated as follows:

$$\sigma_{\max} = \frac{F_{\max}}{A} \tag{3}$$

where σ_{max} is the maximum compressive strength (MPa), F_{max} is the maximum load during loading (N), A is the specimen cross-sectional area (mm^2).

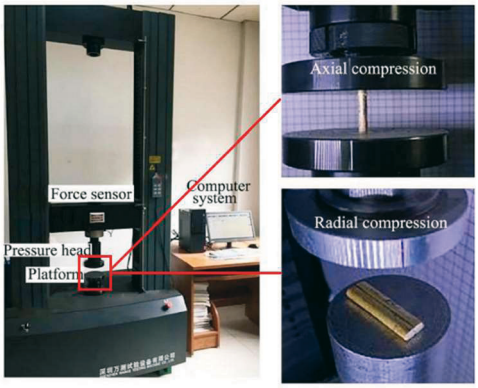

Fig. 8 Quasi-static mechanical test validation

6.1 Axial compression test

Fig. 9 illustrates the damage pattern of the sorghum straw specimens subjected to axial compressive loading. The specimens with knuckle features exhibited uniform rupture, with cracks halting at the knuckle features in the outer skin. Notably, the lower half of the knuckle remained intact and did not fracture or compress. This behaviour indicates that the knuckle feature plays a role in inhibiting crack propagation. During axial compression, the maximum stress value reached approximately 66.51 MPa. D stands for downward distance.

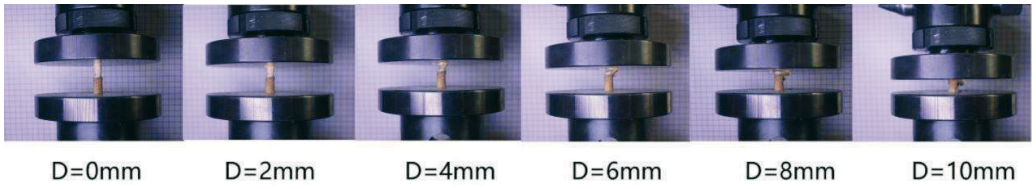

Fig. 9 Axial compression process of sorghum straw

6.2 Radial compression test

Fig. 10 illustrates the damage pattern of the sorghum straw under radial compression. Even when fractures occur, the node features of the straw remain connected. This phenomenon can be attributed to the dense arrangement of fibres at the nodes, which serve to maintain structural integrity. During radial compression, the maximum stress value reached approximately 1.62 MPa. D stands for downward distance.

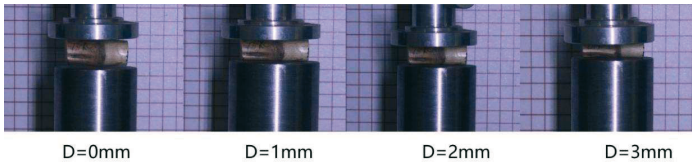

Fig. 10 Radial compression process of sorghum straw

Table 3 presents a comparison between the simulation results and the experimental test values for both the simplified 3D model and the composite 3D model. The simplified 3D model shows a maximum error of 22.15% and a minimum error of 16.67%. In contrast, the composite 3D model exhibits a maximum error of 14.33% and a minimum error of 10.77%. These results indicate that the finite element model developed from the composite 3D model, which incorporates the straw microstructure and CT inverse reconstruction, more closely aligns with

the experimental values. Consequently, the simulation results based on the composite 3D model provide a reliable estimation of force distribution during axial and radial compression of straw, as well as predictions regarding potential failure sites.

Table 3 Comparison of simulation and test maximum stress values

Compression mode	Axial compression					Radial compression				
Norm	Test value (MPa)	Simplified model simulation value (MPa)	Simplified model simulation value error (%)	Composite model simulation value (MPa)	Composite model simulation value error (%)	Test value (MPa)	Simplified model simulation value (MPa)	Simplified model simulation value error (%)	Composite model simulation value (MPa)	Composite model simulation value error (%)
Sorghum straw	7.59	6.31	16.67	6.77	10.77	1.29	1.51	17.32	1.43	11.17

7. Conclusion

This study investigates the microstructure and mechanical properties of sorghum straw through an integrated microscopic and computational approach. SEM and micro-CT reverse reconstruction revealed a tripartite structure: an outer bark, porous basic tissue (pith core), and vascular bundles. Vascular bundles decrease in size and increase in density from the inner to the outer layers, with smaller bundles concentrated internally and larger ones near the bark. The pith core exhibits a foamy, uniform texture, tightly integrated with the thickened nodal regions of the bark.

Using 3D modelling software, two digital models (composite and simplified) were reconstructed to simulate axial and radial compression behaviours using the finite element analysis. Axial compression tests showed maximum stresses of 3,282 MPa (epidermis) and 1,565 MPa (core), with stress gradients influenced by groove geometry and porous core structure. Radial compression yielded higher epidermal stress (4,304 MPa) due to the load concentration at contact points. The porous core reduced stress transmission, resulting in lower residual stresses (25–55 MPa). Comparative validation demonstrated model accuracy, with errors of 14.33% (composite) and 10.77% (simplified) relative to the experimental data, confirming the superior predictive capability for failure-prone regions of the composite model.

REFERENCES

[1] Liu, J., Zhao, D., Zhao, J. (2020). Study of the cutting mechanism of oil tree peony stem. Forests 11(7), 760. https://doi.org/10.3390/f11070760

[2] Kong, E., Liu, D., Guo, X., et al. (2013). Anatomical and chemical characteristics associated with lodging resistance in wheat. Crop J. 1(1), 43-49. https://doi.org/10.1016/j.cj.2013.07.012

[3] Shah, L., Yahya, M., Shah, S.M.A., et al. (2019). Improving lodging resistance: using wheat and rice as classical examples. Int. J. Mol. Sci. 20(17), 4211. https://doi.org/10.3390/ijms20174211

[4] Stubbs, C.J., Sun, W., Cook, D.D. (2019). Measuring the transverse Young's modulus of maize rind and pith tissues. J. Biomech. 84, 113-120. https://doi.org/10.1016/j.jbiomech.2018.12.028

[5] Nona, K.D., Lenaerts, B., Kayacan, E., Saeys, W. (2014). Bulk compression characteristics of straw and hay. Biosyst. Eng. 118, 194-202. https://doi.org/10.1016/j.biosystemseng.2013.12.005

[6] Yu, M., Cannayen, I., Hendrickson, J., et al. (2014). Mechanical shear and tensile properties of selected biomass stems. Trans. ASABE 57, 1231-1242. https://doi.org/10.13031/trans.57.10131

[7] Al-Zube, L., Sun, W., Robertson, D., Cook, D. (2018). The elastic modulus for maize stems. Plant Methods 14, 1-12. https://doi.org/10.1186/s13007-018-0279-6

[8] Mathanker, S.K., Grift, T.E., Hansen, A.C. (2015). Effect of blade oblique angle and cutting speed on cutting energy for energycane stems. Biosyst. Eng. 133, 64-70. https://doi.org/10.1016/j.biosystemseng.2015.03.003

[9] Zhao, Z., Huang, W., Li, B., et al. (2015). Synergistic effects of chiral morphology and reconfiguration in cattail leaves. J. Bionic Eng. 12(4), 634-642. https://doi.org/10.1016/S1672-6529(14)60153-0

[10] Xu, T., Liu, N., Yu, Z., et al. (2017). Crashworthiness Design for Bionic Bumper Structures Inspired by Cattail and Bamboo. Appl. Bionics Biomech. 2017, 5894938. https://doi.org/10.1155/2017/5894938

[11] Xin, Z., Zhang, X., Duan, Y., Xu, W. (2018). Nacre-inspired design of CFRP composite for improved energy absorption properties. Compos. Struct. 184, 102-109. https://doi.org/10.1016/j.compstruct.2017.09.075

[12] Yin, H., Xiao, Y., Wen, G., et al. (2015). Crushing analysis and multi-objective optimization design for bionic thin-walled structure. Mater. Des. 87, 825-834. https://doi.org/10.1016/j.matdes.2015.08.095

[13] Hundertmark, C., Tinter, R., Ortelt, M., Hauser, M.J.B. (2015). Diatom-inspired Plastic Deformation Elements for Energy Absorption in Automobiles. J. Bionic Eng. 12(4), 613-623. https://doi.org/10.1016/S1672-6529(14)60151-7

[14] Liu, Q., Ma, J., He, Z., et al. (2017). Energy absorption of bio-inspired multi-cell CFRP and aluminum square tubes. Compos. Part B-Eng. 121, 134-144. https://doi.org/10.1016/j.compositesb.2017.03.034

[15] Tasdemirci, A., Akbulut, E.F., Güzel, E., et al. (2018). Crushing behavior and energy absorption performance of a bio-inspired metallic structure. Thin-Walled Struct. 131, 547-555. https://doi.org/10.1016/j.tws.2018.07.051

[16] Ha, N.S., Lu, G., Xiang, X. (2018). High energy absorption efficiency of thin-walled conical corrugation tubes mimicking coconut tree configuration. Int. J. Mech. Sci. 148, 409-421. https://doi.org/10.1016/j.ijmecsci.2018.08.041

[17] Song, J., Li, G., Liu, Y., Zou, M. (2024). Quasi-Static and Dynamic Mechanical Properties of Reed Straw. Lat. Am. J. Solids Struct. 21(2), e534. https://doi.org/10.1590/1679-78257991

[18] Mengistie, E.; Bokros, N.; DeBolt, S.; McDonald, A.G. (2024). Lodging Variability in Sorghum Stalks. Crops 4, 3-26. https://doi.org/10.3390/crops4010002

[19] Kar, J.; Rout, A.K.; Sutar, A.K.; Mohanty, T. (2020). Study on static and dynamic mechanical properties of hybrid palm stalk fiber reinforced epoxy composites. BioResources 15, 4249-4270. https://doi.org/10.15376/biores.15.2.4249-4270

[20] Bayable, M.; Tsunekawa, A.; Haregeweyn, N., et al. (2020). Biomechanical Properties in Ethiopian Teff. Agronomy 10, 1012. https://doi.org/10.3390/agronomy10071012

[21] Kumar, A.; Antil, S.K.; Rani, V., et al. (2020). Characterization on Physical, Mechanical, and Morphological Properties of Indian Wheat Crop. Sustainability 12, 2067. https://doi.org/10.3390/su12052067

[22] Oswaldo, E.; Joseph, E.J.; Nayomi Z.P., et al. (2023). Quasistatic and Dynamic Nanoindentation Measurements. Forests 14, 1900. https://doi.org/10.3390/f14091900

[23] Qin, Y., Wang, H. (2023). Prototype, Diversity, and Mixture: The Experience of Commercial Complex Development in Singapore. New Archit. 4, 76-81.

[24] Melati, R.B.; Sass, D.C.; Pagnocca, F.C.; Brienzo, M. (2021). Anatomic influence of sugarcane biomass on xylan solubilization. Ind. Crops Prod. 164, 113357. https://doi.org/10.1016/j.indcrop.2021.113357

[25] Gomez, F.; Mullet, J.; Muliana, A., et al. (2020). The genetic architecture of biomechanical traits in sorghum. Crop Sci. 60, 82-99. https://doi.org/10.1002/csc2.20049

Submitted: 19.11.2024

Accepted: 03.6.2025

Guoyu Li*
Yexuan Luo
School of Mechanical Engineering, Shanghai Dianji University, Shanghai, 201306, People's Republic of China
*Corresponding author:
ligy@sdju.edu.cn